

Correspondence

A New Method for Analyzing Local Shape in Three-Dimensional Images Based on Medial Axis Transformation

Alexandra Bonnassie, Françoise Peyrin, and Dominique Attali

Abstract—In this paper, we propose a new approach based on three-dimensional (3-D) medial axis transformation for describing geometrical shapes in three-dimensional images. For 3-D-images, the medial axis, which is composed of both curves and medial surfaces, provides a simplified and reversible representation of structures. The purpose of this new method is to classify each voxel of the three-dimensional images in four classes: boundary, branching, regular and arc points. The classification is first performed on the voxels of the medial axis. It relies on the topological properties of a local region of interest around each voxel. The size of this region of interest is chosen as a function of the local thickness of the structure. Then, the reversibility of the medial axis is used to deduce a labeling of the whole object. The proposed method is evaluated on simulated images. Finally, we present an application of the method to the identification of bone structures from 3-D very high-resolution tomographic images.

Index Terms—3-D image, bone structure, geometry, microtomography, medial axis, topology.

I. INTRODUCTION

Three-dimensional (3-D) image analysis is raising increasing interest in computer vision. In particular, in medicine, many new tomographic imaging modalities are now producing 3-D images of organs, and the exploitation of such images requires specific methods.

In this context, shape analysis is an important issue. For this purpose, skeletonization is a convenient tool to get a simplified representation of shapes preserving most topological information. It was first introduced by Blum [1] for shape description and features extracted from skeletons are commonly used for pattern recognition, in two-dimensional (2-D) image analysis. Applications of these techniques are ranging from biological cell studies [2], to character recognition [3]. While skeletons and their applications have extensively been studied for 2-D images [4], considerably less work was devoted to 3-D images. In general, 3-D skeletons are not restricted to curves, but are composed both of curves and medial surfaces. Intuitively, curves correspond to cylindrical parts in the object and medial surfaces to planar parts. The interconnections between cylindrical parts and planar parts in the object correspond to branching points in the skeletons. To be a good representation of shapes, skeletons should be centered within the object, should preserve the topology and be reversible. Thus, in principle, skeletons can be used to characterize completely the local geometry and topology of the 3-D object.

Different equivalent definitions of skeletons have been proposed [5]. While these definitions are theoretically equivalent, their implementation may yield to different results, which do not necessarily satisfy all the desired properties. The skeleton may be either represented by a set of points with real coordinates in continuous methods or by a set of voxels computed directly from 3-D discrete images in discrete methods. Continuous methods construct the skeleton from the Voronoi graph of the polygonal approximation of the object boundary [6], [7]. Discrete methods include different approaches. A first one is based on “prairie fire” models, where skeletons correspond to the intersections of propagating wavefront initiated from the object boundary [8]. In a second approach, the skeleton is found from the local maxima of a distance map also known as medial axis [9]. The medial axis has the advantage to be centered within the object but this technique does not generally provide a connected skeleton. Finally, another class of method is based on thinning [10] and [11]: the object boundary is sequentially removed under some conditions, which generally guaranty the preservation of the topology. During this procedure, the “simple points,” i.e., the points whose removal does not modify the object topology, are sequentially deleted. The iterations are stopped when there is no more removal. The remaining nonsimple points are the skeleton points.

Different ways of characterizing simple points in three-dimensional images have been studied [12] and [13]. Moreover, several methods have also been proposed to characterize skeleton points [14]. Saha presented a method for classifying skeleton points in nine different types including arc, surface and different types of junction points [15]. The key idea of these classifications is to compute topological features in a $3 \times 3 \times 3$ neighborhood of each voxel. Topological features include the number of connected components or the Euler number.

However, problems in practical use of skeleton-based representations is that, in one hand, they are not uniquely defined and that in another hand, that they are not very robust to noise. Small irregularities on the object boundary generate parasite branches, which may lead to confusing representations. The sensitivity to noise is even higher when objects are composed of large structures. This requires using simplification methods for keeping only the points thought as representative. This drawback may yield misleading classifications of skeleton points. For instance, the skeleton points of an elliptic cylinder, even if the elliptic cross section is very close from a circle, will be recognized as surface points, while at a macroscopic scale they should rather be interpreted as arc points.

In this paper, we propose a skeleton-based analysis to characterize all the points of a 3-D binary image in four different types. Compared to previously proposed methods, our approach is based on the use of a medial axis transform and does require neither a reconnection, nor a simplification step. First, the points of the medial axis are classified according to their local topological properties, and, then, this classification is extended to the whole 3-D volume. As opposed to the previous approaches, the topological features are evaluated on a subset of the object rather than a subset of the skeleton. Furthermore the size of this subset is automatically adapted to the local thickness at the given point as will be explained in the following. After the description of the method and its implementation, we present its evaluation on simulated 3-D images. Then, the method is investigated to analyze physical 3-D microtomographic images of bone samples.

Manuscript received November 20, 2001; revised February 6, 2003. This work is in the scope of the scientific topics of the PRC-GDR ISIS research Group of the French National Center for Scientific Research (CNRS). This paper was recommended by Guest Editor V. Murino.

A. Bonnassie and F. Peyrin are with CREATIS, CNRS Research Unit (UMR 5515), 69621 Villeurbanne Cedex, France, and also with the European Synchrotron Radiation Facility (ESRF), 38043 Grenoble Cedex, France (e-mail: francoise.peyrin@creatis.insa-lyon.fr).

D. Attali is with the LIS Laboratory, Domaine Universitaire, 38042 Saint-Martin d'Hères, France.

Digital Object Identifier 10.1109/TSMCB.2003.814298

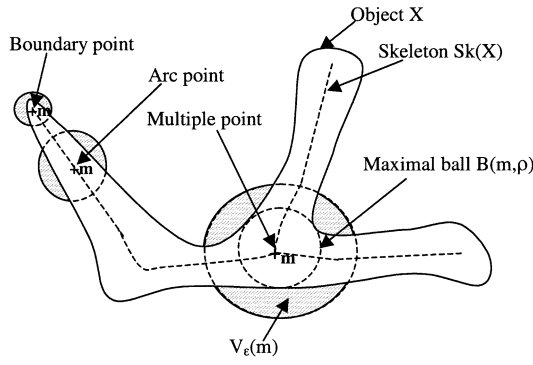


Fig. 1. Illustration of the skeleton of an object X and of some different types of points: boundary, arc and multiple points. The hashed regions around each point m of the skeleton represent the sets $V_\epsilon(m)$ on which the topologic analysis will be performed.

II. CLASSIFICATION METHOD

Let R^3 be the Euclidean 3-D space, d , the Euclidean distance, and X an object in R^3 . The skeleton of an object X provides a synthetic representation of X . The skeleton of X can be defined using the notion of maximal ball. A ball B is said to be maximal in X if for any ball $B', B \subset B' \subset X \Rightarrow B = B'$. The skeleton $Sk(X)$ of X is the locus of the center of the maximal balls of X . The skeleton so defined possesses many attractive mathematical properties such as reversibility, homotopy, and invariance through translations and rotations [16]. In R^2 , the skeleton is a set of curves centered in X and sometimes called medial axis. The points of the medial axis may be easily identified as arc points, multiple points or boundary points as illustrated in Fig. 1. In R^3 , the skeleton is composed of surfaces and curves.

A. Classification of Medial Axis

The purpose of our classification is to identify four types of points on the 3-D skeleton

- Type 1: Boundary points
- Type 2: Branching points
- Type 3: Regular points
- Type 4: Arc points

(1)

Let m be a point on $Sk(X)$. A point m of the skeleton is said to be regular if there exists a neighborhood of m on the skeleton homeomorphic to a disk. We call m a boundary point if it has a neighborhood homeomorphic to a half-disk. We call m an arc point if it has a neighborhood homeomorphic to a curve. Otherwise, the point m is called a branching point.

The idea is to retrieve the type of m by considering a local region of interest around m . Let $B(m)$ be the maximal ball centered at m . It is worthwhile noticing that the intersection between $B(m)$ and the object surface allows us to classify m . To be more specific, if the intersection is composed of two (resp. three or more) points, m is a regular (resp. a multiple) point. If the intersection is a circle, m is an arc point. If the intersection is composed of one point, m is a boundary point. Each connected component of the intersection having the same homotopy type as a point (resp. circle) is considered as a simple point (resp. circle) in the classification.

However, if the surface of the object is irregular, its skeleton will be noisy, and such an approach may fail. Thus we propose to analyze an augmented sphere $B_\epsilon(m)$ to bring some tolerance in the process. Let $\rho(m)$ be the radius of the maximal sphere $B(m)$, and $B_\epsilon(m)$, a sphere centered at m of radius $\rho_\epsilon(m) > \rho(m)$. Let $C_\epsilon(m)$ be the connected component of $B_\epsilon(m) \cap X$ containing m . We define $V_\epsilon(m)$

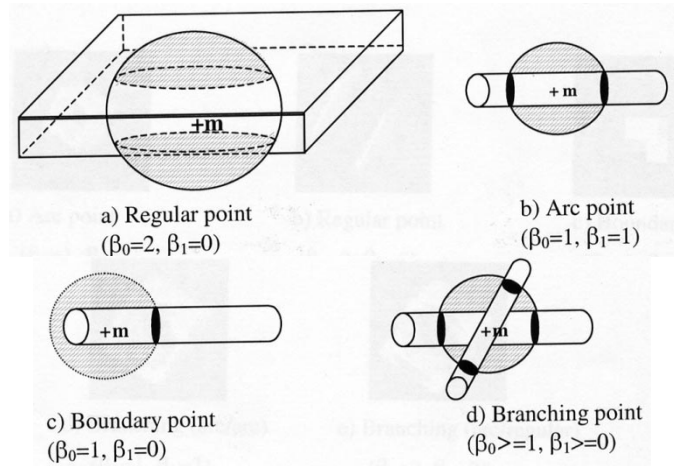


Fig. 2. Topological characteristics of the sets $V_\epsilon(m)$ (hashed region) for the four different types of points. β_0 and β_1 are, respectively, the number of connected component and the Euler number of the sets $V_\epsilon(m)$.

TABLE I
CLASSIFICATION OF THE SKELETON POINT ACCORDING TO THE VALUES OF THE NUMBER OF THE CONNECTED COMPONENT $\beta_0(V_\epsilon(M))$ AND THE EULER NUMBER $\beta_1(V_\epsilon(M))$

$\beta_0(V_\epsilon(m)) \backslash \beta_1(V_\epsilon(m))$	1	2	> 2
0	Boundary	Regular	Branching
1	Arc	Branching regular/arc	Branching regular/arc
>1	Branching arc/arc	Branching regular/arc	Branching regular/arc

as the complement of $C_\epsilon(m)$ in $B_\epsilon(m)$. The appearance of the set $V_\epsilon(m)$ for different points of the skeleton is illustrated in Fig. 2.

The analysis will be based on the characterization of the topological properties of sub-volume $V_\epsilon(m)$. These properties will be inferred from the Betti numbers and the Euler Characteristics of $V_\epsilon(m)$ [17]. The Euler Number χ of a volume V is a topological invariant related to the Betti Numbers via the following relationship:

$$\chi(V) = \beta_0(V) - \beta_1(V) + \beta_2(V) \quad (2)$$

where $\beta_0(V)$, $\beta_1(V)$, and $\beta_2(V)$ are respectively the Betti numbers representing the number of connected components, the number of loops (tunnels), and the number of voids in V .

We assume that the volume contains no isolated component. In this case, the Euler Number of any sub-volume $V_\epsilon(m)$ reduces to

$$\chi(V_\epsilon(m)) = \beta_0(V_\epsilon(m)) - \beta_1(V_\epsilon(m)) \quad (3)$$

The proposed classification of $V_\epsilon(m)$ is based on its characteristics $\beta_0(V_\epsilon(m))$, and $\beta_1(V_\epsilon(m))$ as presented in Table I.

Fig. 2 represents typical sets $V_\epsilon(m)$ associated to the four classes of points, and the corresponding values of $\beta_0(V_\epsilon(m))$ and $\beta_1(V_\epsilon(m))$.

Using this procedure, an integer label, $L(m)$, between one and four, is assigned to each point m of $Sk(X)$ according to its type as defined in (1).

B. Classification of the Whole Three-Dimensional Volume

The reversibility property, which allows recovering the whole 3-D volume from its skeleton, is a crucial assumption in our method. More precisely, the 3-D volume may be reconstructed from its skeleton from

$$X = \cup \{B(m) / m \in Sk(X)\} \quad (4)$$

We propose to use the same idea to extend the classification of the skeleton points to the whole object by propagating the labels to the entire maximal balls. For this purpose, we need to assign an order relation

to the different labels. We choose the order of the list (1) presented in Section IIA, to privilege arc and regular points, which generally correspond, to the geometric primitives of interest. Each point m will receive the largest label of the skeleton points, whose maximal sphere contains m . The labeling of each point m of X , will thus be performed from the following relationship:

$$L(m) = \max\{L(m')/m' \in \text{Sk}(X) \text{ and } m \in B(m')\} \quad (5)$$

III. IMPLEMENTATION

The implementation of the proposed method requires its transposition to discrete space. The object space is now defined on a finite domain I of \mathbf{Z}^3 . Each voxel in Ω is defined by its centroid (i, j, k) and is assumed to have a value equal to zero or one. The discrete binary object X is the set of voxels having for value one, assumed to be nonempty. Let \bar{X} , be the complement of X .

A. Discrete Medial Axis

The algorithm first requires the 3-D discrete medial axis of the binary image, but also the radius of the maximal ball in each of its point. For this purpose, a convenient tool is to use computations based on distance maps. Note that such computations do not necessarily conserve the connectivity relationships but preserve the reversibility, which is more important in our context. If the Euclidian distance is a natural choice in continuous space, its use for discrete images poses the problem of manipulating floating point values. Discrete distances have been proposed to overcome this drawback and enable working with integers. In 3-D, if distances such as d_6 or d_{26} are conventional and simple, Chamfer distances permits to obtain better approximations of the Euclidean distance [9]. Chamfer distances are based on the principle that the value of the distance at a voxel may be deduced from the value of the distance at its neighbors. The simplest Chamfer distances in 3-D is defined by a set of integers (a, b, c) such that the Chamfer distance d_c between two voxels $p = (p_1, p_2, p_3)$ and $q = (q_1, q_2, q_3)$ is defined by

$$d_c(P, Q) = c \min(P, Q) + b(\text{med}(P, Q) - \min(P, Q)) + a(\max(P, Q) - \text{med}(P, Q)) \quad (6)$$

where $\min(P, Q)$, $\max(P, Q)$, and $\text{med}(P, Q)$ are respectively the minimum, maximum, and median value of $\{|q_i - p_i|/i = 1, 3\}$. Although it is possible to use more elaborated chamfer masks [18], we used the chamfer mask $(a, b, c) = (3, 4, 5)$ which is a good compromise between precision and computing time.

The distance map is defined at each voxel x of the object X , as its distance to the nearest voxel of \bar{X} , i.e.,

$$d(x, \bar{X}) = \min\{d(x, y)/y \in \bar{X}\} \quad (7)$$

We used an iterative construction of the distance map. The computation of the 3-D medial axis was then performed from the local maxima of the discrete distance map by following a similar procedure as suggested in [19] for 2-D images. The radius of the maximal ball at each voxel of the medial axis is given by the value of the distance map at this voxel. The knowledge of the medial axis, and of the associated radius ensures the reversibility of this representation. The diameter of the maximal balls may also be called the local thickness of the structure by analogy with the definition given in [20]. Note that the local thickness may be computed at any voxel of X by using the reversibility property. For this purpose, the following procedure is applied. The voxels m , of the medial axis, are scanned by increasing radius $\rho(m)$. For each voxel m , the value $\rho(m)$ is assigned to all the voxels contained in the maximal ball centered at m , i.e.,

$$\text{For each } m', \text{ such that } d(m, m') < \rho(m) \rho(m') = \rho(m) \quad (8)$$

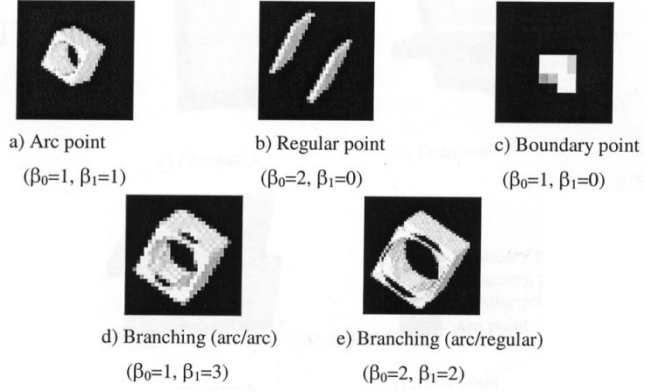


Fig. 3. Examples of local ROIs corresponding to the four different types of points in a discrete 3-D image, and their computed topological characteristics. β_0 is the number of connected component and β_1 , the Euler number.

B. Topological Analysis

The next step of the algorithm involves topological analysis. Different adjacency relationships are commonly defined in 3-D discrete space: in 6- (resp. 18, 26) connectivity, a voxel possesses 6 (resp. 18, 26) connected neighbors. As was pointed out by Kong and Rosenfeld [13], choosing the same topology for the object and its background leads to a paradox. A conventional choice of dual topologies are (26, 6) or (6, 26), respectively, for the object and the background.

Our algorithm requires the computation of the Euler number $\chi(V_\varepsilon(m))$ and of the number of connected components $\beta_0(V_\varepsilon(m))$. The number of connected components of $V_\varepsilon(m)$, $\beta_0(V_\varepsilon(m))$, is computed in 26-connectivity by using a labeling in connected components [21]. The transposition of the properties of the Euler number from the continuous case to digital pictures was established in [22]. It is shown that the Euler characteristics is equal to the number of connected components minus the number of tunnels and plus the number of cavities. The computation of the Euler number of a finite polyhedron V , may be performed by using the following general decomposition for any triangulation K :

$$\chi(V) = \sum_i (-1)^i n_i \quad (9)$$

where n_i is the number of i -simplexes in K .

This decomposition may be applied by choosing respectively n_0, n_1, n_2, n_3 , as the numbers of pointels (vertices), linels (edges), surfels (faces), and voxels of the binary object. Each element is counted only once. The topologic characteristics (number of connected components and Euler number) of discrete sets $V_\varepsilon(m)$ calculated for different types of points are illustrated in Fig. 3.

C. Extension of the Labeling to the Whole Volume

The labeling of the medial axis is extended to the whole volume according to relation (5). The computation is similar to the computation of the local thickness map. The algorithm is the following:

For each Label L
 For each radius r
 $\text{Sk}(r) = \{m \in \text{Sk}(X)/\rho(m) = r\}$
 For each voxel $m \in \text{Sk}(r)$
 For each voxel $m' \in B(m, r)$
 $L(m') = L(m)$

The result is dependent of the order in which the label is scanned, since the highest labels will overlap the lowest. This order was selected to privilege regular and arc types.

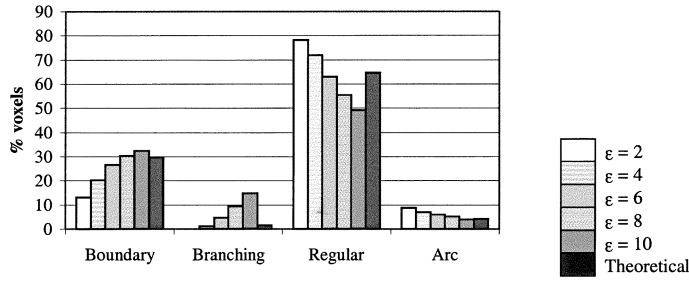


Fig. 4. Percentages of the four types of points obtained with the proposed method in Phantom5 composed of three cylinders and two planes for different values of ϵ . The expected theoretical percentage is also plotted (black) for comparison.

IV. RESULTS

The algorithm was first tested on five simulated 3-D images, generated from simple geometric shapes. Their different sizes are expressed in voxel units. Phantom 1 is made of one cylinder (diameter: 11, height: 64), and Phantom 2, of two orthogonal cylinders (diameters: 9 and 19, length: 64). Phantom 3 consists in a single plate (thickness: 11, width: 64, height: 64), and Phantom 4 is composed of two orthogonal plates. Phantom 5 presents a mixture of the different shapes: two parallel plates ($6 \times 110 \times 110$ and $10 \times 110 \times 110$) perpendicular to three cylinders (diameters: 7, 11, 7, length: 91).

A. Size of Neighborhood $B_\epsilon(m)$

The application of the proposed algorithm first requires fixing the size of the local neighborhood $B_\epsilon(m)$ considered around each voxel of the medial axis. This size is chosen larger than $\rho(m)$ (the radius of maximal ball centered in m) as $\rho_\epsilon(m) = \rho(m) + \epsilon$. The algorithm was tested for different values of ϵ , ranging between two and ten (expressed in voxel unit). For each configuration, the respective percentages of boundary, branching, regular and arc points were evaluated. Since the phantom is composed of simple geometrical shapes, we also estimated the theoretical percentages of each class. Fig. 4 shows the resulting percentages obtained on Phantom 5 for the different values of ϵ , as well as the theoretical percentage.

Increasing the size of the analysis ball ($\epsilon > 4$) results in amplifying the number of boundary or/and branching voxels. Consequently, the numbers of arc or/and regular voxels are underestimated. Thus the augmentation of the radius should be limited to minimize this effect. However, the choice of the smallest value ($\epsilon = 2$) involves an important overestimation of the regular voxels because the analysis ball does not correctly include the local structure. The value $\epsilon = 4$ seems to be a good compromise between the different choices to handle complex phantoms not restricted to a single cylinder or a single plate.

B. Results on Different Phantoms ($\epsilon = 4$)

The results of the classification of the different phantoms for $\epsilon = 4$ are displayed in 3-D in Fig. 5. To visualize the results, we assigned a gray level to the different labels as follows: boundary: 50, branching: 100, regular: 150, arc: 200 (the color code is displayed in Fig. 5). Note that the main types of the different structures are correctly rendered for all phantoms. To get a more quantitative assessment of the method, the differences between the percentage estimated from our algorithm and the theoretical values are reported in Table II. We do not expect to recover exactly the theoretical values due to discretization errors, but they are taken as an indicator of the behavior of the method. Both

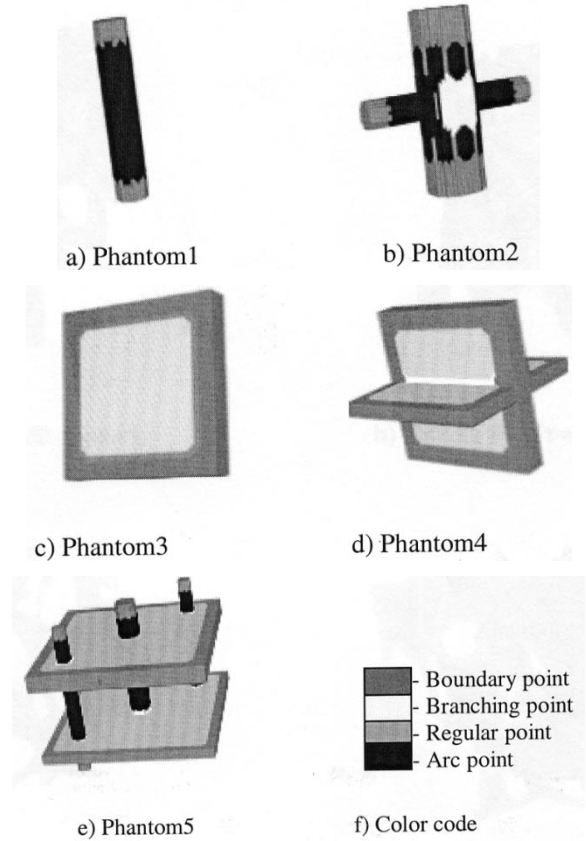


Fig. 5. 3-D displays of the classified volumes for the different phantoms ($\epsilon = 4$). The boundary, branching, regular and arc points are respectively coded with the color code displayed on the bottom.

TABLE II
QUANTITATIVE PERCENTAGES OF THE FOUR TYPES OF POINTS OBTAINED FOR THE FIVE PHANTOMS ($\epsilon = 4$). FOR EACH PHANTOM, THE FIRST AND THE SECOND LINES OF THE TABLE SHOW RESPECTIVELY THE THEORETICAL AND EXPERIMENTAL PERCENTAGES. THE LAST LINE OF THE TABLE CORRESPONDS TO THE DEVIATION BETWEEN THEORETICAL AND EXPERIMENTAL PERCENTAGES

phantom	class	Boundary	Branching	Regular	Arc
Phantom1	theoretical	36,5%	0%	0%	63,5%
	Experimental	19,6%	0%	0%	80,4%
	deviation	16,9%	0%	0%	-16,9%
Phantom2	theoretical	25,6%	5,4%	0%	69,0%
	Experimental	27,8%	4,8%	0%	67,4%
	deviation	-2,2%	0,6%	0%	1,6%
Phantom3	theoretical	24,8%	0%	75,2%	0%
	Experimental	36,0%	0%	64,0%	0%
	deviation	-11,2%	0%	11,2%	0%
Phantom4	theoretical	32,0%	5,7%	62,3%	0%
	Experimental	36,6%	5,2%	58,2%	0%
	deviation	-4,6%	0,5%	4,1%	0%
Phantom5	theoretical	29,5%	1,6%	64,7%	4,2%
	Experimental	20,2%	1,1%	71,8%	7,0%
	deviation	9,3%	0,5%	-7,1%	-2,8%

Fig. 5 and Table II evidence that the boundary class is generally overestimated because of the size of the analyzing neighborhood (Phantom 2, 3, 4). Thus, what is recovered is a boundary much thicker than one voxel. This is particularly visible at the top and bottom of the cylindrical shapes. In the case of Phantom 1 and Phantom 5, this is not true because the order chose in the extension of the labeling process overlap the boundary points. The boundary points will be all the more overestimated that the structure is thick. The errors on the boundaries have

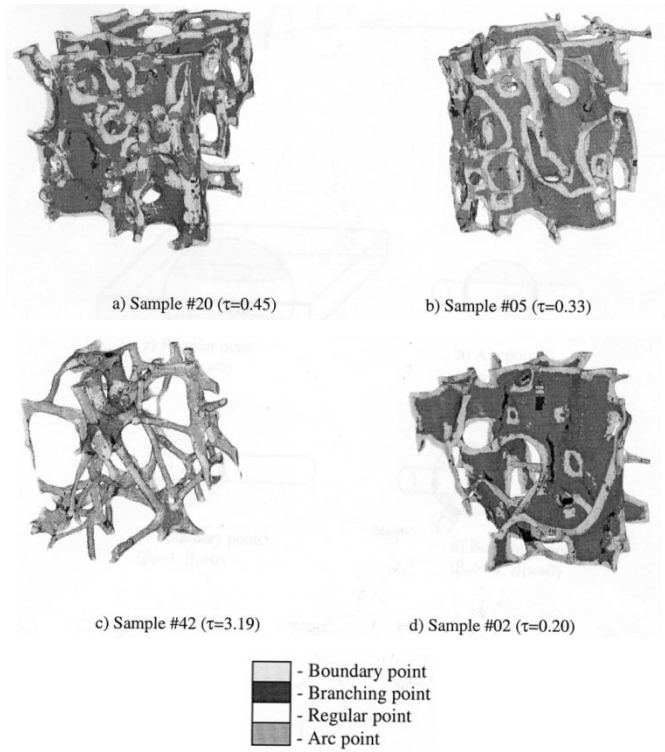


Fig. 6. Three-dimensional displays of the classification applied to 3-D x-ray μ CT bone samples. The samples #20 (resp. #42) contains mainly plate-like (resp. rod-like) structures. Each label appears in a given color (see correspondence at the bottom).

a direct repercussion on the percentage of arc or regular points, which will subsequently be underestimated (Phantoms 2, 3, 4) or overestimated (Phantoms 1, 5). We note that the deviation between theoretical and experimental percentages of the structure of interest (arcs and regular) is weak. Moreover, in the case of phantom 5, which is a mixture of rods and plates, the estimated percentages of regular and arc points are in the same orders of magnitude as the theoretical ones.

V. APPLICATION TO THREE-DIMENSIONAL BONE CT IMAGES

The proposed method was applied to 3-D images of bone structures obtained from X-ray microtomography (μ CT) [23]. Indeed the characterization of trabecular bone architecture is important to understand the evolution of the structure with diseases such as osteoporosis, and its relationships to biomechanical properties of bone [24], [25]. Bone structures are typically made of plates or rods, or of a mixture of these components. The determination of the main type of structures, or of the respective ratios of plates and rods within the bone volume, may be an indicator of interest relatively to its biomechanical strength.

While many studies have been devoted to the morphometric analysis of bone structures, few works deal with topological or geometrical characterization [26], [27]. In [28], a global index, called structure model index (SMI) has been proposed to classify the structure as plate-like or rod-like or of bone structure. Plate-like structures corresponds to a $SMI < 1$, while rod-like structure are characterized by a higher SMI value.

Due to the small size of bone trabeculae ($\sim 100 \mu m$), the imaging of bone micro-architecture requires very high-resolution techniques. For this purpose, we used synchrotron radiation μ CT images acquired at the ESRF with a voxel size of $6.7 \mu m$ [23]. Eleven bone samples ($7 mm$)³ were cut out from lumbar vertebrae in normal women with different

TABLE III
QUANTITATIVE PERCENTAGES OF THE FOUR TYPES OF POINTS OBTAINED FOR THE ELEVEN 3-D BONE μ CT IMAGES ($\varepsilon = 4$). THE CLASSIFICATION RESULTS ARE STORED ACCORDING TO THE INCREASING AGE OF THE PATIENTS

	Years	Boundary	Branching	Regular	Arc
#20	33	14,22%	1,09%	58,54%	26,15%
#30	47	10,25%	5,11%	78,90%	5,75%
#83	48	14,34%	3,81%	68,62%	13,23%
#50	53	15,15%	3,26%	66,36%	15,23%
#26	55	17,37%	2,55%	57,66%	22,43%
#24	60	11,98%	2,89%	78,60%	6,53%
#05	63	18,49%	2,86%	58,99%	19,65%
#45	71	22,29%	0,86%	51,24%	25,61%
#42	72	7,32%	1,23%	21,79%	69,65%
#02	82	18,21%	3,22%	65,25%	13,32%
#65	93	16,54%	0,93%	54,55%	27,99%

ages. 512³ images were reconstructed from 900 radiographic images of the sample rotated by angular steps of 0.2° . At this spatial resolution, the typical thickness of trabeculae is around 15 voxels. The 3-D binary volumes were first segmented by simple thresholding, which was sufficient due to the high spatial resolution. The images were then pre-processed to suppress parasitic isolated voxels, which did not correspond to features of interest (a 6-connectivity was used). Fig. 6 displays the results of the analysis for four human vertebral samples drawn out from women of different ages: #20 (33 years), #05 (63 years), #42 (72 years) and #02 (82 years). The color code displayed at the bottom of Fig. 6 was used to visualize the four labels. In all images, the points labeled, as arc and plate, are correctly localized. In the samples #20 [Fig. 6(a)] and #42 [Fig. 6(c)], showing typical plate-like and rod-like bone structures, the dominant types of the structure are correctly assessed from the method. The quantitative results on all samples are presented on Table III. The percentages of plates and rods in these images are respectively 58% and 26%, for the plate-like bone and 22% and 70% for the rod-like bone.

In order to compare our results to the SMI method, we estimated the ratio τ between the volumes of arcs (rods) V_r and of regular voxels (plates) V_p from each method. The SMI is indeed related to this ratio for the following formula [28]:

$$SMI = 12 \cdot \frac{\tau + \tau^2}{1 + 4(\tau + \tau^2)} \quad (10)$$

where $\tau = V_r/V_p$.

The ratios derived from each method on the eleven human vertebral samples were significantly correlated ($r^2 = 0.98$, $p < 10^{-9}$). Although both methods are quite different, the results are in agreement. The proposed method enables supplementary insight into bone structure since the analysis is local.

VI. CONCLUSION

In this paper, we proposed a new method for analyzing the shapes in a 3-D binary image from a topological analysis. The approach consists in labeling the individual voxels of the structure as boundary, branching, regular or arc points based on a local topological analysis. As opposed to other methods, our approach makes simultaneously use of the 3-D object and of its skeleton. In addition, instead of working on $3 \times 3 \times 3$ neighborhood of each voxel, we analyze a larger neighborhood. An originality of the method is that the size of the local analysis region is automatically adapted to the local thickness of the structure. The method was implemented by computing a reversible 3-D medial axis

of the object, based on a discrete distance map transform. The classification performed on the medial axis could have been exploited directly. However, we proposed to extend this classification to the total volume by propagating the labels. At this step, we made an arbitrary choice by choosing an order relation on the labels, which was coherent with our foreseen applications. The evaluation on simulated images shows that the main structures of interest are correctly labeled, although due to the principle of the method, boundary points tend to be overestimated for the largest structures. In future, the boundary points could be eliminated by reassigning them to the class of the nearest neighbors. This method is of particular interest to analyze the shapes of bone structures mainly composed of rods and plates. The results obtained on bone images at very high spatial resolution are coherent with those given by the global SMI index. The method will be applied to the analysis of different series of bone samples representative of a pathology or a response to a therapy. In future works, this low-level classification could be exploited to get a more structured representation of bone structures in terms on geometrical cylindrical or plate primitives. For instance, such descriptions could be of great interest to reduce the computational cost of finite element codes applied to high-resolution images to simulate biomechanical properties of bone structure.

ACKNOWLEDGMENT

The authors wish to acknowledge A. M Laval-Jeantet for providing the vertebra samples, M. Salomé, and the ID19 group for help during data acquisition of μ CT images of the European Synchrotron Radiation facility (ESRF), Grenoble, France.

REFERENCES

- [1] H. Blum, "Transformation for extracting new descriptors of shapes," in *Models for the Perception of Speech, and Visual Form*, W. Walthen-Dunn, Ed. Cambridge, MA: MIT Press, 1967, pp. 362–380.
- [2] E. Thiel and A. Montanvert *et al.*, "Shape splitting from medial lines using the 3–4 chamfer distance," in *Visual Form Analysis and Recognition*, C. Arcelli *et al.*, Eds. New York: Plenum, 1992, pp. 537–546.
- [3] R. C. Gonzalez and R. E. Woods, *Digital Image Processing*. Reading, MA: Addison Wesley, 1992.
- [4] L. Lam, S. W. Lee, and C. Y. Suen, "Thinning methodologies—A comprehensive survey," *IEEE Trans. Pattern Anal. Machine Intell.*, vol. 14, pp. 869–885, Sept. 1992.
- [5] U. Montanari, "A method for obtaining skeletons using a quasi Euclidean distance," *J. ACM*, vol. 15, pp. 600–624, 1968.
- [6] D. Attali and A. Montanvert, "Computing and simplifying 2-D and 3-D semicontinuous skeletons of 2-D and 3-D shapes," *Comput. Vis. Image Understand.*, vol. 67, no. 3, pp. 261–273, Sept. 1997.
- [7] J. W. Brandt and V. R. Algari, "Continuous skeleton computation by Voronoi diagram," *Comput. Vis. Graph. Image Process.*, vol. 55, no. 3, May 1992.
- [8] C. Arcelli, I. P. Cordella, and S. Levialdi, "From local maxima to connected skeletons," *IEEE Trans. Pattern Anal. Machine Intell.*, vol. 3, pp. 134–142, Mar. 1981.
- [9] E. Thiel, "Les distances de chanfrein en analyses d'images: fondements et applications," Ph.D. dissertation, Université Joseph Fourier, Grenoble I, France, 1994.
- [10] T. C. Lee, R. L. Kashyap, and C. N. Chu, "Building skeleton models via 3-D medial surface/axis thinning algorithms," *Comput. Vis. Graph. Image Process.*, vol. 56, no. 6, pp. 462–478, 1994.
- [11] P. K. Saha and B. B. Chaudhuri, "3-D Digital topology under binary transformation with applications," *Comput. Vis. Image Understand.*, vol. 63, no. 3, pp. 418–429, May 1996.
- [12] G. Bertrand and G. Malandain, "A new characterization of three-dimensional simple points," *Pattern Recognit. Lett.*, vol. 15, pp. 169–175, 1994.
- [13] T. Y. Kong and A. Rosenfeld, "Digital topology: Introduction and survey," *Comput. Vis. Graph. Image Process.*, vol. 48, pp. 357–393, 1989.
- [14] G. Malandain, G. Bertrand, and N. Ayache, "Topological classification in digital space," in *Proc. 12th Int. Conf. Information Processing Medical Imaging*, New York, July 1991, pp. 300–313. LNCS 511.
- [15] P. K. Saha and B. B. Chaudhuri, "A new shape preserving parallel thinning algorithm for 3-D digital images," *Discrete Applied Math.*, vol. 21, pp. 67–79, 1988.
- [16] G. Matheron, "Examples of topological properties of skeletons," in *Image Analysis and Mathematical Morphology*, J. Serra, Ed. New York: Academic Press, vol. 2.
- [17] M. Henle, *A Combinatorial Introduction to Topology*. New York: Dover, 1994.
- [18] G. Borgefors, "Distance transformation in arbitrary dimensions," *Comput. Vis., Graph. Image Process.*, vol. 27, pp. 321–145, 1984.
- [19] E. Remy and E. Thiel, "Optimizing 3-D chamfer masks with distance constraints," presented at the Nth7-IWCIA, Int. Workshop Combinatorial Image Analysis, 2000.
- [20] T. Hildebrand and P. Rüeggsegger, "A new method for the model-independent assessment of thickness in three-dimensional images," *J. Microsc.*, vol. 185, no. 1, pp. 67–75, Jan. 1997.
- [21] J. M. Chassery and A. Montanvert, *Géométrie discrète en analyse d'images*, Hermes, Paris, France, 1991.
- [22] T. Y. Kong, A. W. Roscoe, and A. Rosenfeld, "Concepts of digital topology," *Top. Appl.*, vol. 46, 1992.
- [23] M. Salomé, F. Peyrin, P. Cloetens, C. Odet, A. M. Jeantet, B. Baruchel, and P. Spanne, "A synchrotron radiation microtomography system for the analysis of trabecular bone samples," *Med. Phys.*, vol. 26, no. 10, pp. 2194–2204, Oct. 1999.
- [24] T. M. Link, S. Majumdar, J. C. Lin, D. C. Newitt, P. Augat, X. Ouyang, A. Mathur, and H. K. Genant, "A comparative study of trabecular bone properties in the spine and femur using high resolution MRI and CT," *J. Bone Mineral Res.*, vol. 13, no. 1, pp. 122–132, 1998.
- [25] J. Kabel, A. Odgaard, V. Rietbergen, and R. Huiskes, "Connectivity and elastic properties of cancellous bone," *Bone*, vol. 24, no. 2, pp. 115–120, Feb. 1999.
- [26] P. K. Saha, B. R. Gomberg, and F. W. Wehrli, "Three-dimensional digital topological characterization of cancellous bone architecture," *Int. J. Imaging Syst. Technol.*, vol. 11, pp. 81–90, 2000.
- [27] L. Pothuau, P. Porion, E. Lespessailles, C. L. Benhamou, and P. Levitz, "A new method for three-dimensional skeleton graph analysis of porous media: Application to trabecular bone microarchitecture," *J. Microsc.*, vol. 199, no. 2, pp. 149–161, 2000.
- [28] T. Hildebrand and P. Rüeggsegger, "Quantification of bone microarchitecture with the structure model index," *Comput. Methods Biomech. Biomed. Eng.*, vol. 1, pp. 15–23, 1997.